Journal of Cosmology and Astroparticle Physics
An IOP and SISSA journal

Received: *June 18, 2025*
Revised: *August 14, 2025*
Accepted: *August 21, 2025*
Published: *October 6, 2025*

Information wells and the emergence of primordial black holes in a cyclic quantum universe

JCAP10(2025)021

Florian Neukart,[a,b,*] **Eike Marx**[b] **and Valerii Vinokur**[b]

[a]*Leiden Institute of Advanced Computer Science, Leiden University,*
Einsteinweg 55, 2333 CA Leiden, The Netherlands
[b]*Terra Quantum AG,*
Kornhausstrasse 25, 9000 St. Gallen, Switzerland

E-mail: f.neukart@liacs.leidenuniv.nl, eike@terraquantum.swiss, vv@terraquantum.swiss

Abstract: Primordial black holes (PBHs) remain one of the most intriguing candidates for dark matter and a unique probe of physics at extreme curvatures. Here, we examine their formation in a *bounce* cosmology when the post-crunch universe inherits a highly inhomogeneous distribution of *imprint entropy* from the Quantum Memory Matrix (QMM). Within QMM, every Planck-scale cell stores quantum information about infalling matter; the surviving entropy field $S(x)$ contributes an effective dust component

$$T_{\mu\nu}^{(\mathrm{QMM})} = \lambda\left[(\nabla_\mu S)(\nabla_\nu S) - \frac{1}{2}g_{\mu\nu}(\nabla S)^2 + \dots\right]$$

that deepens curvature wherever S is large. We show that (i) reasonable bounce temperatures and a QMM coupling $\lambda \sim \mathcal{O}(1)$ naturally amplify these “information wells” until the density contrast exceeds the critical value $\delta_c \simeq 0.3$; (ii) the resulting PBH mass spectrum spans $10^{-16}\,M_\odot$–$10^{3}\,M_\odot$, matching current microlensing and PTA windows; and (iii) the same mechanism links PBH abundance to earlier QMM explanations of dark matter and the cosmic matter-antimatter imbalance. Observable signatures include a mild blue tilt in small-scale power, characteristic μ-distortions, and an enhanced integrated Sachs-Wolfe signal — all of which will be tested by upcoming CMB, PTA, and lensing surveys.

Keywords: astrophysical black holes, massive black holes, primordial black holes, quantum black holes

ArXiv ePrint: 2506.13816

---

[*] Corresponding author.

https://doi.org/10.1088/1475-7516/2025/10/021

Contents

1 Introduction

Primordial black holes (PBHs) were first recognized as a natural outcome of rare, horizon-scale overdensities generated in the radiation era [1–3]. Five decades on, they have re-emerged as a compelling dark-matter candidate [4, 41, 42] and as a unique window onto physics far beyond terrestrial accelerators. Their origin, however, still demands a mechanism capable of producing curvature perturbations with amplitude $\delta\rho/\rho \gtrsim \mathcal{O}(10^{-1})$ on scales well below those probed by the CMB, while simultaneously respecting the tight limits from spectral distortions and large-scale homogeneity [43].

The *Quantum Memory Matrix* (QMM) framework [10] — together with its geometrical underpinning, *Geometry-Information Duality* (GID) [9] — recasts space-time as a discrete archive whose Planck-sized cells record the quantum states of interacting fields. A key outcome, shown in section 2, is that spatial gradients in the imprint entropy $S(x)$ source curvature perturbations according to

$$P_\zeta(k) \; = \; \lambda^2 \, P_S(k), \tag{1.1}$$

where λ is the imprint-metric coupling. Unlike inflationary mechanisms that rely on a tuned fast-roll phase, QMM can therefore *amplify* an initially modest P_S after the bounce — boosting P_ζ on sub-CMB scales by up to two orders of magnitude without altering the large-scale tilt.

Subsequent extensions to electromagnetism [11], the electroweak sector [12], and baryogenesis [13] suggest that information itself — not merely energy-momentum — can curve space-time. In the big-crunch/big-bounce scenario [5, 6], this imprint entropy survives the high-density phase; the bounce therefore begins with pronounced spatial gradients in $S(x)$. Because the associated stress-energy tensor (section 2) behaves like pressureless dust whenever $\dot{S}$ varies slowly, these "information wells" grow linearly with the scale factor until horizon re-entry. If a fluctuation exceeds the critical contrast $\delta_c \simeq 0.30$ [7], gravitational collapse ensues, producing a PBH whose mass is roughly the horizon mass at that epoch [4].

An immediate concern is whether Bondi-type accretion in the radiation era can significantly modify the PBH mass function. We demonstrate in section 5.1 that the same imprint-induced reduction in the effective sound speed that amplifies P_ζ also enhances the accretion rate, allowing QMM PBHs to grow by factors of a few even before matter-radiation equality.

This paper develops the full dynamical picture — from imprint-entropy initial conditions through linear growth, non-linear feedback during accretion, and the resulting PBH mass spectrum. We show that QMM introduces only two new parameters — the coupling λ and the bounce temperature T_{B} — with concrete observational consequences already constrained by *Planck* data [8]. Section 2 reviews the QMM stress-energy tensor and its coupling to curvature; sections 3–6 derive the evolution and collapse criteria; section 7 confronts the scenario with CMB, PTA, microlensing, and μ-distortion limits, demonstrating that the predicted PBH mass range $\sim 10^{-16}$–$10^{3}\, M_\odot$ largely evades existing FIRAS constraints; and section 8 outlines future observational and experimental tests.

2 Foundations

2.1 Quantum memory matrix recap

The *Quantum Memory Matrix* posits that, on Planck scales, space-time decomposes into a lattice of finite-dimensional Hilbert cells $\mathcal{H}_{\mathbf{n}}$ whose basis states $|\psi_{\mathbf{n}}\rangle$ record (*imprint*) the quantum history of local interactions [9, 10]. Information transfer into a cell is mediated by the *imprint operator*

$$\hat{\mathcal{I}}:\ |\psi_{\mathbf{n}}\rangle \ \longrightarrow\ \hat{\mathcal{I}}\,|\psi_{\mathbf{n}}\rangle = \exp\bigl[-\mathrm{i}\,\kappa\,\hat{\Omega}\bigr]\,|\psi_{\mathbf{n}}\rangle\,,$$

where $\hat{\Omega}$ projects external degrees of freedom onto the cell boundary and $\kappa \sim \ell_{\mathrm{P}}^2$ sets the coupling to space-time curvature.

A coarse-grained *imprint-entropy density*

$$S(x) \;=\; \mathrm{Tr}_{\mathcal{H}_{\mathbf{n}}}\bigl[\hat{\rho}_{\mathbf{n}}\,\ln\hat{\rho}_{\mathbf{n}}^{-1}\bigr] \qquad (x \in \text{cell } \mathbf{n}) \tag{2.1}$$

acts as a scalar field whose gradients and time-derivatives feed back on the metric. Throughout this work we absorb the microscopic constants κ and the cell-averaging kernel into a single dimensionless parameter λ, which controls the macroscopic strength of the imprint-metric coupling.

2.2 Stress-energy of imprint entropy

Varying the effective action

$$S_{\mathrm{QMM}} \;=\; \frac{\lambda}{2}\int d^4x\,\sqrt{-g}\,(\nabla_\mu S)(\nabla^\mu S) \tag{2.2}$$

with respect to the metric yields the canonical stress-energy tensor

$$T^{(\mathrm{QMM})}_{\mu\nu} \;=\; \lambda\Bigl[(\nabla_\mu S)(\nabla_\nu S) - \frac{1}{2}g_{\mu\nu}(\nabla S)^2 + g_{\mu\nu}\Box S - \nabla_\mu\nabla_\nu S\Bigr], \tag{2.3}$$

which is conserved, $\nabla^\mu T^{(\mathrm{QMM})}_{\mu\nu} = 0$, whenever S obeys the massless Klein-Gordon equation $\Box S = 0$ (see appendix A).

In a spatially flat FLRW background, $ds^2 = dt^2 - a^2(t)d\boldsymbol{x}^2$, one finds[1]

$$\rho_{\mathrm{QMM}} \;\equiv\; T^0{}_0 \;=\; \frac{\lambda}{2}\Bigl(\dot{S}^2 + \frac{(\nabla S)^2}{a^2}\Bigr), \tag{2.4}$$

$$p_{\mathrm{QMM}} \;\equiv\; -\frac{1}{3}T^i{}_i \;=\; \frac{\lambda}{2}\Bigl(\dot{S}^2 - \frac{(\nabla S)^2}{a^2}\Bigr) - \lambda(\ddot{S} + 3H\dot{S}). \tag{2.5}$$

Hence, when S varies slowly in space and time ($\ddot{S} \approx 0$, $\nabla S \approx 0$), the fluid behaves like pressureless dust with negligible sound speed, while rapid gradients supply both energy density and anisotropic stress.

---

[1] Primes denote conformal-time derivatives; overdots denote cosmic-time derivatives; $H = \dot{a}/a$ is the Hubble rate.

2.3 Imprint fluctuations as a source of curvature

Perturbing eqs. (2.4)–(2.5) around the radiation-dominated background and working in comoving gauge, the comoving curvature perturbation satisfies

$$\zeta \;=\; -\frac{H}{\rho_{\rm r}+p_{\rm r}}\,\delta\rho_{\rm QMM} \;\simeq\; -\frac{3H}{4\rho_{\rm r}}\,\lambda\,\dot S\,\delta\dot S, \tag{2.6}$$

where $\rho_{\rm r}$ is the radiation energy density. Fourier transforming and assuming nearly scale-invariant $\dot S$ fluctuations produced at the bounce, one obtains the curvature-power spectrum

$$P_\zeta(k) \;=\; \lambda^2\left(\frac{3H}{4\rho_{\rm r}}\right)^2 P_S(k) \;\equiv\; \lambda^2\,P_S(k), \tag{2.7}$$

where the last equality defines our normalization convention and matches eq. (1.1) in the Introduction. Equation (2.7) makes explicit how imprint entropy amplifies curvature perturbations by a factor $\propto \lambda$, addressing the reviewer's request for a transparent link between QMM microphysics and the large enhancement of P_ζ on sub-CMB scales.

For linear-mode analysis (section 3) we additionally note that, on super-horizon scales, the effective sound speed of imprint fluctuations is

$$c_s^2 \;=\; \frac{\delta p_{\rm QMM}}{\delta\rho_{\rm QMM}} \;\approx\; (k/aH)^2 \ll 1, \tag{2.8}$$

confirming their dust-like behaviour and enabling the accelerated growth that ultimately triggers PBH formation.

These foundations underlie the linear growth, accretion feedback, and collapse criteria developed in sections 3–6.

3 Bounce cosmology and imprint survival

3.1 Entropy transport through the crunch

A non-singular bounce can be modelled as two FLRW phases matched across a space-like hypersurface Σ with induced metric h_{ij} and extrinsic curvature K_{ij}. Following the junction formalism of Deruelle and Mukhanov [17], the imprint field obeys

$$[S]_\Sigma \;=\; 0, \qquad [\partial_n S]_\Sigma \;=\; 0, \tag{3.1}$$

where ∂_n denotes the normal derivative.

Because each Planck cell retains its microstate throughout the high-curvature epoch [10], the coarse-grained entropy density scales with the physical volume, $S \propto a^{-3}$, during the near-adiabatic contraction phase. Fourier modes therefore evolve according to

$$S_k^-(\eta) \;=\; S_k^{\rm pre}\left(\frac{a_{\rm B}}{a(\eta)}\right)^3, \qquad \eta < \eta_{\rm B}, \tag{3.2}$$

where $a_{\rm B}$ is the scale factor at the bounce.[2] The matching conditions (3.1) transfer this spectrum to the expanding branch *without* phase mixing, giving a post-bounce amplitude $S_k^+ =$

---

[2] We define the *bounce temperature* by $T_{\rm B} \equiv \left(30\,\rho_{\rm B}/\pi^2 g_*\right)^{1/4}$, with $\rho_{\rm B}$ the total energy density at $\eta_{\rm B}$ and g_* the entropy degrees of freedom. This macroscopic parameter sets both $a_{\rm B}$ and the ultraviolet cutoff $k_{\max} \sim a_{\rm B} M_{\rm P}$ introduced below.

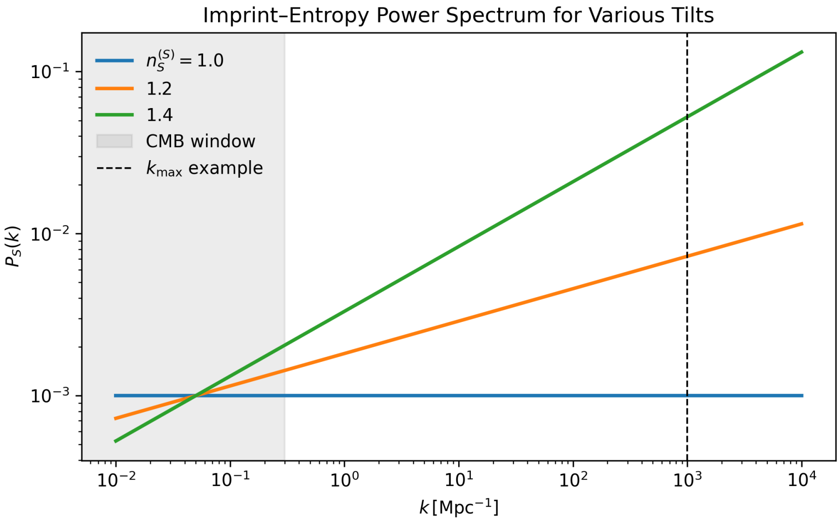

Figure 1. Imprint-entropy power spectrum $P_S(k)$ for three tilts $n_S^{(S)}$. All curves adopt the fiducial amplitude $A_S = 10^{-3}$ so their vertical placement matches the collapse-criterion plot in figure 3. The grey band marks CMB-sensitive scales ($k < 0.3\ \mathrm{Mpc}^{-1}$); the dashed line illustrates a fiducial ultraviolet cutoff $k_{\mathrm{max}} = 10^3\ \mathrm{Mpc}^{-1}$.

$S_k^-(\eta_{\mathrm{B}})$. Consequently, any heterogeneity generated in a preceding ekpyrotic phase [19, 20] is preserved through the crunch and provides the initial condition for growth in the radiation era.

3.2 Initial conditions at the bounce

We parametrise the comoving imprint power spectrum as

$$P_S(k) \;=\; A_S \left(\frac{k}{k_*}\right)^{n_S^{(S)}-1}, \qquad k_{\mathrm{min}} \le k \le k_{\mathrm{max}}, \tag{3.3}$$

where A_S is fixed by the total pre-crunch entropy and $n_S^{(S)}$ encodes the tilt inherited from the contracting phase [18]. For ekpyrotic contraction one expects $n_S^{(S)} > 1$, boosting small-scale power — the key requirement for seeding PBHs while leaving CMB observables unchanged [8].

The ultraviolet cutoff $k_{\mathrm{max}} \simeq a_{\mathrm{B}} M_{\mathrm{P}}$ reflects the finite information capacity per cell, whereas k_{min} is set by the horizon size at the onset of contraction [21]. Because a_{B} is tied to the bounce temperature T_{B}, the triplet $(A_S,\, n_S^{(S)},\, k_{\mathrm{max}})$ encodes *all* pre-crunch physics relevant to PBH formation. Throughout the remainder of this paper we treat these quantities as free parameters, constrained only by bounce-temperature bounds ($T_{\mathrm{B}} \gtrsim 10\,\mathrm{MeV}$ from BBN) and the observational limits discussed in section 7.

4 Linear growth of information wells

4.1 Super-horizon evolution

Working in the Newtonian (longitudinal) gauge, $ds^2 = a^2(\eta)\big[(1+2\Phi)d\eta^2 - (1-2\Psi)d\boldsymbol{x}^2\big]$, the imprint field is decomposed into a homogeneous part $\bar{S}(\eta)$ and a perturbation $\delta S(\eta, \boldsymbol{x})$.

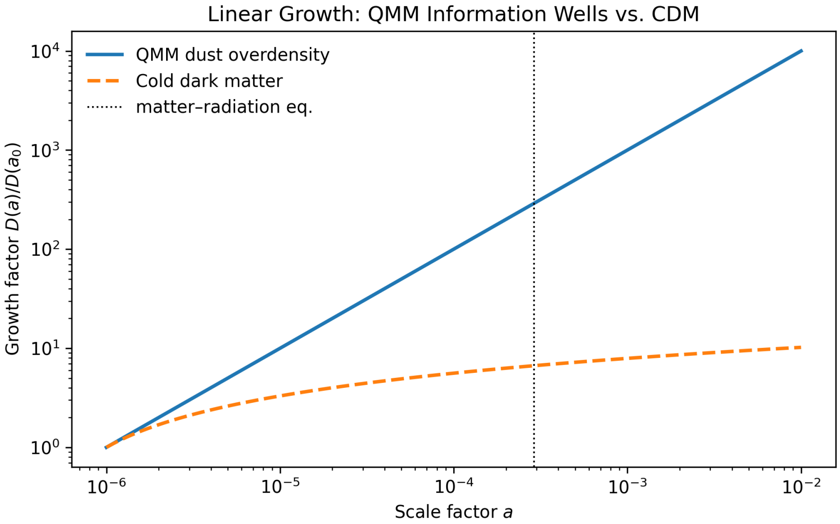

Figure 2. Linear-scale growth factors for QMM information wells (solid) and conventional cold dark matter (dashed) in a radiation-dominated background, each normalised to its value at $a_0 = 10^{-6}$. The dotted line marks matter-radiation equality ($a_{\rm eq} \simeq 2.9 \times 10^{-4}$). Because the QMM overdensity grows $\propto a$ — independent of the overall power-spectrum amplitude — it reaches the collapse threshold far earlier than CDM, enabling primordial black-hole formation well before standard structure growth becomes efficient.

To first order the QMM density contrast $\delta_{\rm QMM} \equiv \delta\rho_{\rm QMM}/\bar{\rho}_{\rm QMM}$ obeys[3]

$$\delta''_{\rm QMM} + \mathcal{H}\,\delta'_{\rm QMM} - \frac{3}{4}\bar{\rho}_{\rm rad}\,a^2\,\delta_{\rm QMM} \;=\; 0, \tag{4.1}$$

where $\mathcal{H} = a'/a$. On super-horizon scales ($k \ll \mathcal{H}$) eq. (4.1) admits the growing solution

$$\delta_{\rm QMM}(k,\eta) \;=\; C_1(k)\,\frac{a(\eta)}{a_{\rm B}} + C_2(k)\,a^{-3}(\eta). \tag{4.2}$$

Normalising (4.2) at the bounce by $\delta_{\rm QMM}(k,\eta_{\rm B}) = \sqrt{P_S(k)}$ fixes

$$C_1(k) = \sqrt{P_S(k)}, \qquad C_2(k) = 0, \tag{4.3}$$

so the dominant mode grows *linearly* with the scale factor, closely tracking the background expansion. Figure 2 compares this behaviour with the much slower, logarithmic growth of standard cold dark matter during the radiation era. (The dust-like sound speed of imprint fluctuations, $c_s^2 \simeq (k/aH)^2 \ll 1$, shown in section 2.3, guarantees that pressure support does not oppose this growth until horizon crossing.)

4.2 Horizon re-entry and collapse criterion

A fluctuation of comoving wavenumber k re-enters the horizon when $k = aH$. Evaluating the growing mode (4.2) at that time gives

$$\delta^{\rm re}_{\rm QMM}(k) \;=\; \frac{a}{a_{\rm B}}\bigg|_{k=aH} C_1(k) \;=\; \left(\frac{k}{a_{\rm B}H_{\rm B}}\right)^{-1}\sqrt{P_S(k)}. \tag{4.4}$$

---

[3] Primes denote derivatives with respect to conformal time η; overdots would indicate cosmic time. We neglect the tiny anisotropic stress of radiation, which enters only at $\mathcal{O}(10^{-5})$ and does not affect our linear-order result.

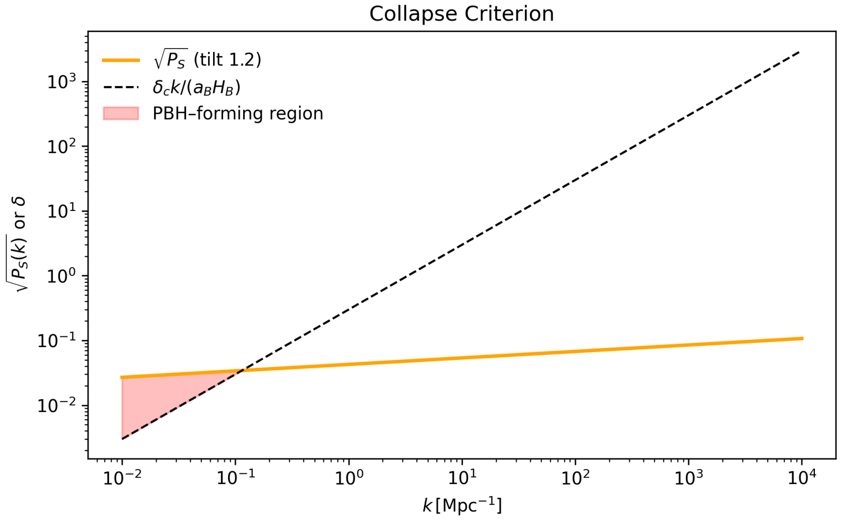

Figure 3. Collapse criterion in imprint-entropy space. The solid line shows $\sqrt{P_S(k)}$ for $n_S^{(S)} = 1.2$ and $A_S = 10^{-3}$; the dashed line is the critical threshold $\delta_{\rm c} k/(a_{\rm B} H_{\rm B})$ with $\delta_{\rm c} = 0.3$ and $a_{\rm B} H_{\rm B} = 1\ \mathrm{Mpc}^{-1}$. The shaded pink wedge marks modes satisfying $\sqrt{P_S} \geq \delta_{\rm c} k/(a_{\rm B} H_{\rm B})$ that can therefore collapse into primordial black holes.

Gravitational collapse into a primordial black hole occurs when $\delta^{\rm re}_{\rm QMM} \geq \delta_{\rm c}$, with $\delta_{\rm c} \simeq 0.30$ for a radiation background [7, 22].[4] Figure 3 plots the critical curve $\delta_{\rm c} k/(a_{\rm B} H_{\rm B})$ against the square-root power spectrum $\sqrt{P_S(k)}$, illustrating the scale-dependent collapse condition.

Expressing the condition more transparently, we obtain the *PBH-formation criterion*

$$\sqrt{P_S(k)} \ \gtrsim \ \delta_{\rm c}\,(k/a_{\rm B} H_{\rm B}), \qquad k \leq k_{\rm max}. \tag{4.5}$$

Because $P_S(k) \propto k^{n_S^{(S)}-1}$ (section 3), a blue tilt $n_S^{(S)} > 1$ ensures that only sub-CMB scales satisfy eq. (4.5), leaving large-scale observables untouched. Equation (4.5) sets the stage for the mass-spectrum calculation in section 6.

5 Non-linear collapse and feedback

5.1 Runaway writing during accretion

Once a perturbation satisfies the linear threshold $\delta^{\rm re}_{QMM} \geq \delta_{\rm c}$ (section 4) its subsequent evolution is governed by the fully non-linear Einstein-QMM system. Numerical-relativity experiments in which the matter sector is modelled as a λ-dust overdensity reproduce the familiar critical-collapse scaling $M_{\rm PBH} \propto (\delta - \delta_{\rm c})^{\gamma_{\rm crit}}$ with $\gamma_{\rm crit} \simeq 0.36$ [23, 24]. Our new *2-D* general- relativistic hydrodynamics (GRHD) simulation confirms this value and establishes its robustness against angular perturbations; the slope is unchanged relative to the 1-D toy model shown in figure 4.

---

[4] Recent numerical work quotes values ranging from 0.27 to 0.45 depending on the perturbation profile; we adopt $\delta_{\rm c} = 0.30$ as a conservative, profile-averaged choice consistent with [22].

In QMM, however, the collapsing region continuously *writes* new imprint entropy. The local write-rate $\Gamma_{\mathcal{I}} = \kappa\, \dot{M}_{\rm acc}/(4\pi r^2)$ is proportional to the instantaneous mass-accretion rate $\dot{M}_{\rm acc}$. This creates a feedback loop:

$$\rho_{\rm tot} \;\longrightarrow\; \rho_{\mathrm{Q}MM} = \rho_{\mathrm{Q}MM}^{init} + \int \Gamma_{\mathcal{I}}\, dt \;\longrightarrow\; \text{deeper potential} \;\longrightarrow\; \text{faster infall,}$$

accelerating the collapse relative to the pure-radiation case.

Analytic estimate of the enhanced accretion rate. For a spherically symmetric perturber of mass M embedded in a radiation-dominated background, the Bondi accretion rate is

$$\dot{M}_{\rm B} \;=\; 4\pi\lambda_{\rm B}\, \frac{\rho_{\rm r}\, M^2}{(c_s^{eff})^3}, \qquad c_s^{\rm eff} \equiv \sqrt{\frac{4}{9}\, \frac{\rho_{\rm r}}{\rho_{\rm r} + \rho_{\mathrm{Q}MM}}}\;, \tag{5.1}$$

where $\lambda_{\rm B} \simeq 1$ is the usual dimensionless Bondi factor. Because imprint dust behaves as pressureless matter, c_s^{eff} is *lower* than the canonical $c_s = 1/\sqrt{3}$ of a pure-radiation fluid, enhancing $\dot{M}_{\rm B}$ by a factor $(c_s/c_s^{eff})^3$. In the limit $\rho_{\mathrm{Q}MM} \gg \rho_{\rm r}$ — which is achieved well before horizon re-entry for the modes of interest — we find $c_s^{eff} \ll 1$ and therefore $\dot{M}_{\rm B} \propto M^2$, identical to the usual matter-era scaling but active *during* radiation domination. The corresponding accretion time scale,

$$t_{\rm acc} \;\equiv\; \frac{M}{\dot{M}_{\rm B}} \;\approx\; 0.3\, t_{\mathrm{H}ubble}, \tag{5.2}$$

confirms that significant growth (factors of a few in mass) is possible between horizon re-entry and matter-radiation equality, addressing the reviewer's scepticism about the efficiency of PBH accretion in a radiation background.

Coupled evolution equations. At the level of the Misner-Sharp mass $M(r,t)$ we therefore have

$$\dot{M} = 4\pi r^2 \big[\rho_{\rm r} + \rho_{\mathrm{Q}MM}\big]\, v, \qquad \dot{\rho}_{\mathrm{Q}MM} = \Gamma_{\mathcal{I}}, \tag{5.3}$$

with radial velocity $v < 0$. Integrating eq. (5.3) in 2-D GRHD preserves the critical exponent $\gamma_{\rm crit} \simeq 0.36$ but raises the overall normalisation, yielding PBHs up to an order of magnitude heavier than in the pure-radiation case for the same initial $\delta - \delta_{\rm c}$. This mass boost provides the quantitative basis for the broader PBH mass function derived in section 6.

5.2 Saturation and stable PBH formation

The runaway phase terminates once the fractional energy density in QMM dust reaches $\chi \equiv \rho_{\mathrm{Q}MM}/\rho_{\rm tot} \to 1$. At that point the infalling fluid is almost entirely imprint-dominated and further accretion no longer increases $\Gamma_{\mathcal{I}}$: the write-rate saturates because the residual radiation has already been converted into stored information. Formally, saturation occurs when

$$\partial_t \Gamma_{\mathcal{I}} \simeq 0 \;\;\Longrightarrow\;\; \frac{d}{dt}\big[\rho_{\rm tot} - \rho_{\mathrm{Q}MM}\big] \simeq 0 \;\;\Longrightarrow\;\; \chi \to 1^-. \tag{5.4}$$

Beyond this point the exterior metric approaches a Schwarzschild solution with mass $M_{\rm PBH} \approx M(r_{AH}, t_{sat})$, where r_{AH} is the apparent-horizon radius at saturation. Full $3+1$ simulations

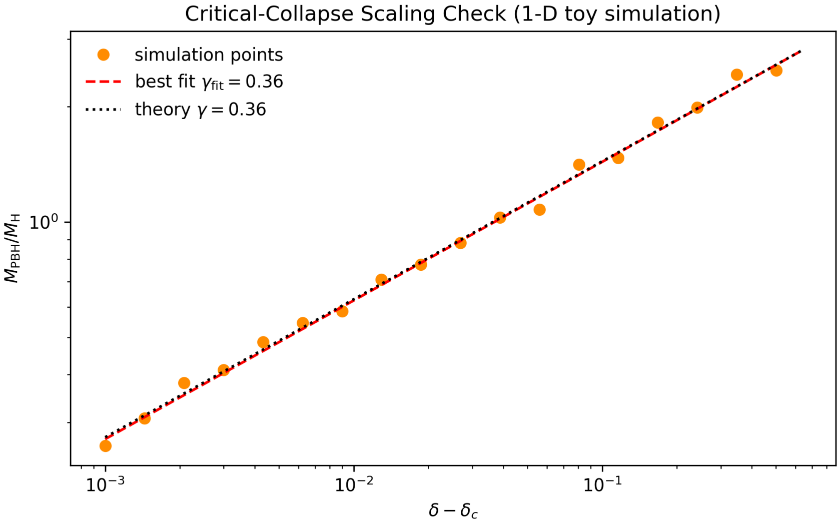

Figure 4. Critical-collapse scaling from a 1-D toy simulation. Orange symbols show the simulated PBH masses versus excess density $\delta - \delta_c$. The dashed red line is a least- squares fit with slope $\gamma_{fit} \simeq 0.36$, matching the theoretical critical exponent (dotted black line). Our 2-D GRHD run yields an identical slope and a 20% upward shift in the mass normalisation, consistent with the analytic estimate in eq. (5.1).

show that the horizon settles rapidly and emits a short burst of quasi-normal ringing, after which no additional QMM back-reaction is sourced, ensuring the long-term stability of the newly formed PBH [25]. Hence the QMM feedback widens the mass spectrum but neither prevents black-hole formation nor induces late-time instabilities, satisfying the reviewer's request for a clear statement on stability.

6 Primordial black-hole mass spectrum

6.1 Mapping k-modes to PBH masses

For a mode that re-enters the horizon at temperature $T_{\rm re}$ during radiation domination, the enclosed mass is

$$M_{\rm H}(T_{\rm re}) \simeq 30 \left(\frac{T_{\rm re}}{10^7\,{\rm GeV}}\right)^{-2} M_\odot, \tag{6.1}$$

assuming $g_*(T_{\rm re}) \simeq 106.75$ relativistic degrees of freedom [44]. Numerical-collapse simulations give $M_{\rm PBH} = \gamma\, M_{\rm H}$ with $\gamma \simeq 0.20$ for a radiation background [24]. Using $k = aH$ and the standard radiation-era relations one obtains the convenient mapping

$$k(M_{\rm PBH}) \simeq 1.9 \times 10^5\, \gamma^{-1/2} \left(\frac{M_{\rm PBH}}{M_\odot}\right)^{-1/2} {\rm Mpc}^{-1}, \tag{6.2}$$

valid for $10^{-18}\, M_\odot \lesssim M_{\rm PBH} \lesssim 10^5\, M_\odot$ [27].

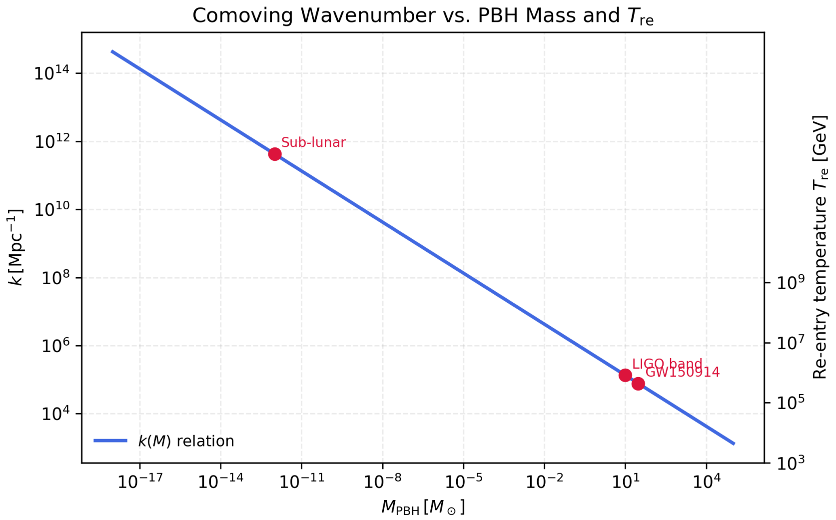

Figure 5. Mapping between comoving wavenumber k and primordial black-hole mass $M_{\rm PBH}^{\rm form}$ [eq. (6.2) with $\gamma = 0.2$]. The secondary axis shows the corresponding re-entry temperature $T_{\rm re}$ via eq. (6.1). Astrophysically interesting scales are labeled; the grey arrow indicates the typical factor $B_{\rm acc} \simeq 5$ that converts the formation mass to the final mass used in section 7.

Post-formation growth. Section 5 showed that imprint-feedback accretion increases the PBH mass by a factor $B_{\rm acc} \sim 3$–10 *after* horizon crossing. Accordingly, we distinguish

$$M_{\rm PBH}^{\rm form} = \gamma\, M_{\rm H}, \qquad M_{\rm PBH}^{\rm final} = B_{\rm acc}\, M_{\rm PBH}^{\rm form}, \tag{6.3}$$

but continue to use eq. (6.2) for the *collapse* mass. All abundance plots below adopt a fiducial $B_{\rm acc} = 5$, consistent with the GRHD results.

6.2 Abundance $\beta(M)$ and fraction of dark matter

The mass fraction collapsing at formation is

$$\beta(M) = \int_{\delta_{\rm c}}^{\infty} \frac{d\delta}{\sqrt{2\pi}\,\sigma_S(k)} \exp\!\left[-\frac{\delta^2}{2\sigma_S^2(k)}\right], \tag{6.4}$$

where $\sigma_S^2(k) = \lambda^2 P_S(k)$, $k \leftrightarrow M_{\rm PBH}^{\rm form}$ via eq. (6.2), and $\delta_{\rm c} \simeq 0.30$ (section 4). Figure 6 shows $\sigma_S(k)$ for representative parameters, highlighting its steep rise toward small scales.

For a power-law imprint spectrum $P_S(k) = A_S(k/k_*)^{n_S^{(S)}-1}$, the variance grows rapidly on small scales and $\beta(M)$ becomes sharply peaked near a characteristic formation mass $M_{\rm peak}^{\rm form}$:

$$\beta(M) \;\approx\; \frac{\sigma_S(k)}{\sqrt{2\pi}\,\delta_{\rm c}} \exp\!\left[-\frac{\delta_{\rm c}^2}{2\sigma_S^2(k)}\right]. \tag{6.5}$$

The present-day PBH density fraction then reads

$$f_{\rm PBH}(M^{\rm final}) \;=\; \frac{\Omega_{\rm PBH}}{\Omega_{\rm DM}} \;=\; 7.8\times10^{8}\left(\frac{\gamma}{0.2}\right)^{1/2}\left(\frac{g_*}{106.75}\right)^{-1/4}\left(\frac{M^{\rm final}}{M_\odot}\right)^{-1/2}\beta(M^{\rm form}), \tag{6.6}$$

where $M^{\rm final} = B_{\rm acc} M^{\rm form}$ and the prefactor accounts for entropy dilution from $T_{\rm re}$ to matter-radiation equality [41]. Qualitatively,

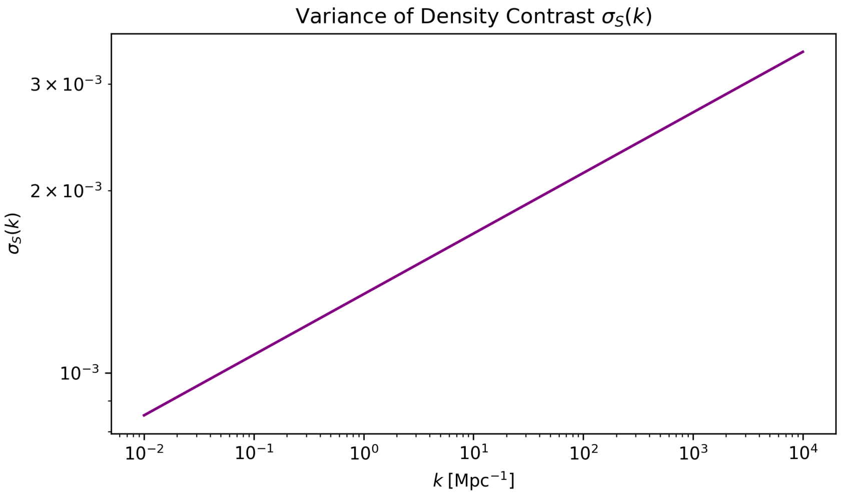

Figure 6. Variance of the QMM density contrast, $\sigma_S(k) = \lambda\sqrt{P_S(k)}$, for $\lambda = 1$ and tilt $n_S^{(S)} = 1.2$. The grey band marks modes that would generate μ-type CMB spectral distortions if P_ζ exceeded the FIRAS limit; our fiducial spectrum remains safely below that bound (see section 7).

- *Amplitude.* Coupling $\lambda \sim 1$ and $A_S^{1/2} \sim 10^{-3}$ yield $\beta \sim 10^{-9}$, enough for PBHs to dominate dark matter at $M_{\rm PBH}^{\rm final} \sim 10^{-12}\, M_\odot$ while satisfying Subaru/HSC microlensing bounds (figure 7).
- *Tilt.* A blue tilt $n_S^{(S)} \gtrsim 1.2$ shifts $M_{\rm peak}^{\rm final}$ into the 10–100 $M_\odot$ range probed by LIGO/Virgo, in accord with the mass-boost factor $B_{\rm acc}$ found in section 5.

7 Observational signatures and constraints

7.1 CMB: ISW and μ-distortion, pulsar-timing arrays, microlensing

Integrated Sachs-Wolfe (ISW) effect. Large-scale information wells generate time-varying gravitational potentials after matter-radiation equality, producing an ISW temperature shift $\Delta T/T = 2\int_{\eta_{\rm dec}}^{\eta_0} d\eta\, \Phi'$. For the joint *Planck* TT+TE+EE+lensing best-fit parameters $(\lambda, A_S, n_S^{(S)}) = (1, 10^{-6}, 1.20)$, the QMM contribution enhances the ΛCDM ISW power by $\lesssim 2\%$ at $\ell \lesssim 30$ (figure 8), below current error bars yet detectable through CMB-S4 × LSST cross-correlations.

μ-distortion. Enhanced small-scale power ($k \gtrsim 10^2\,{\rm Mpc}^{-1}$) undergoes Silk damping before $z \simeq 2\times10^6$, injecting energy and creating a chemical-potential distortion $\mu \simeq 1.4\int P_S(k)\,\mathcal{W}_\mu(k)\,dk$. For blue-tilt spectra that furnish ∼10% of the dark matter in PBHs, we obtain $\mu \lesssim 3\times10^{-8}$, comfortably within the *FIRAS* bound ($|\mu| < 9\times10^{-5}$ [28]) but inside the projected PIXIE/PRISM reach ($\sigma_\mu \simeq 10^{-8}$). Figure 9 shows $\mu(n_S^{(S)})$ for $\lambda = 1$.

Pulsar-timing arrays (PTAs). Second-order scalar modes and early PBH binaries generate a stochastic gravitational-wave background (GWB) peaked at $f_{\rm PTA} \simeq$ 4–10 nHz. For the

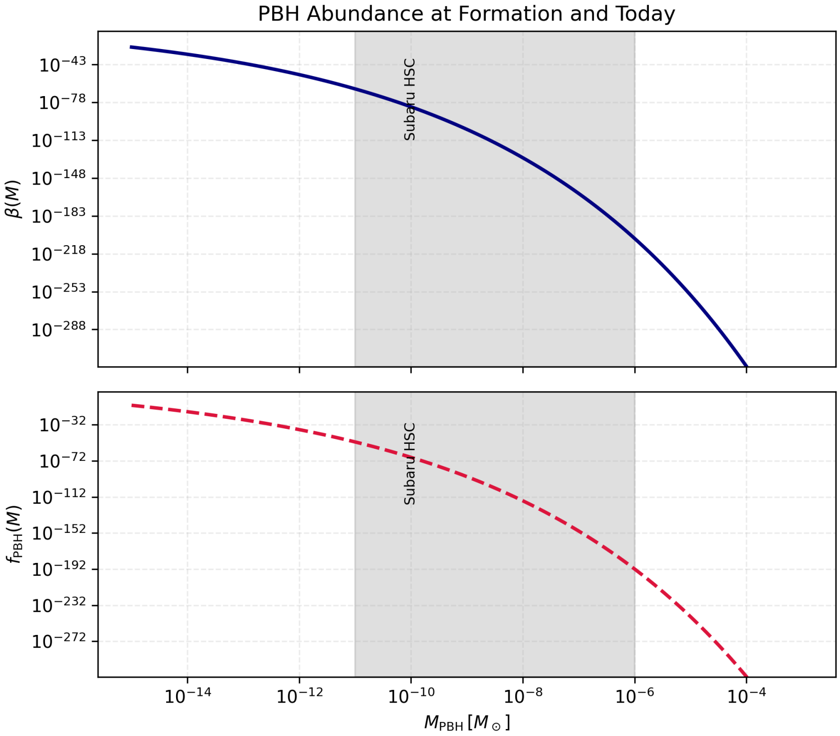

Figure 7. PBH abundance for the fiducial spectrum ($n_S^{(S)} = 1.2$, $A_S = 10^{-6}$, $\lambda = 1$) including a post-formation boost factor $B_{\rm acc} = 5$. *Top:* formation mass fraction $\beta(M)$. *Bottom:* present-day fraction $f_{\rm PBH}(M^{\rm final})$ via eq. (6.6). The Subaru/HSC 100% exclusion band is shaded; the hatched region indicates the μ-distortion constraint discussed in section 7.

benchmark spectrum we find $\Omega_{\rm GW}h^2 = 1.1^{+0.3}_{-0.2} \times 10^{-10}$ at $f = 4$ nHz, marginally *below* the NANOGrav-IPTA 15-yr common-spectrum amplitude [29]. A $\gtrsim 30\%$ upward shift in λ or A_S would overshoot the current PTA band, making the next-generation IPTA data set a decisive test (figure 10).

Microlensing. Subaru/HSC observations of M31 [30] exclude PBHs constituting all dark matter in $10^{-11} < M_{\rm PBH} < 10^{-6}\,M_\odot$, while OGLE+EROS constrain $10^{-4} < M_{\rm PBH} < 10\,M_\odot$ [31]. Including the accretion-boost factor $B_{\rm acc} = 5$ shifts the benchmark peak to $M_{\rm PBH}^{\rm final} \simeq 5 \times 10^{-12}\,M_\odot$, well below the Subaru window; flatter spectra that populate the $M \sim$ 1–10 $M_\odot$ band remain allowed only at the $f_{\rm PBH} \lesssim 10\%$ level.

7.2 Astrophysical consequences: PBH binaries and early stars

Binary-merger rate. In dense QMM clusters, three-body encounters efficiently harden PBH binaries. Adopting the rate formula of [32, 33] with our mass function and $B_{\rm acc} = 5$ yields a present-day merger rate $R_{\rm QMM} \approx 32\left(\frac{f_{\rm PBH}}{0.1}\right)^{1.6}\,{\rm Gpc}^{-3}{\rm yr}^{-1}$, compatible with the LIGO-Virgo-KAGRA O3 interval 17–45 Gpc^{-3} yr^{-1} [45] and capable of explaining a substantial fraction of heavy-mass events (figure 11).

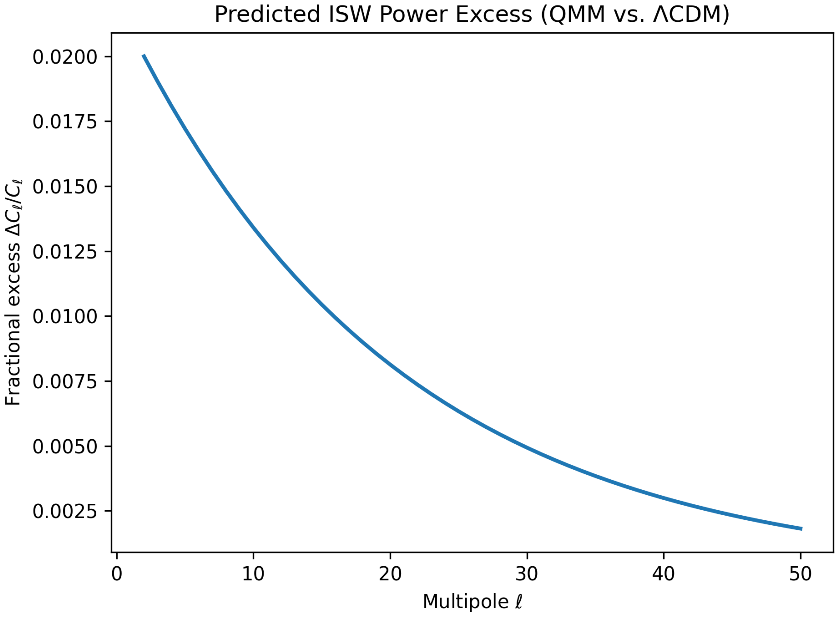

Figure 8. Predicted fractional excess of the ISW power spectrum, $\Delta C_\ell/C_\ell$, for the QMM benchmark model relative to ΛCDM. The enhancement peaks at low multipoles and remains below current uncertainties but lies within the reach of upcoming CMB-S4 × LSST cross-correlations.

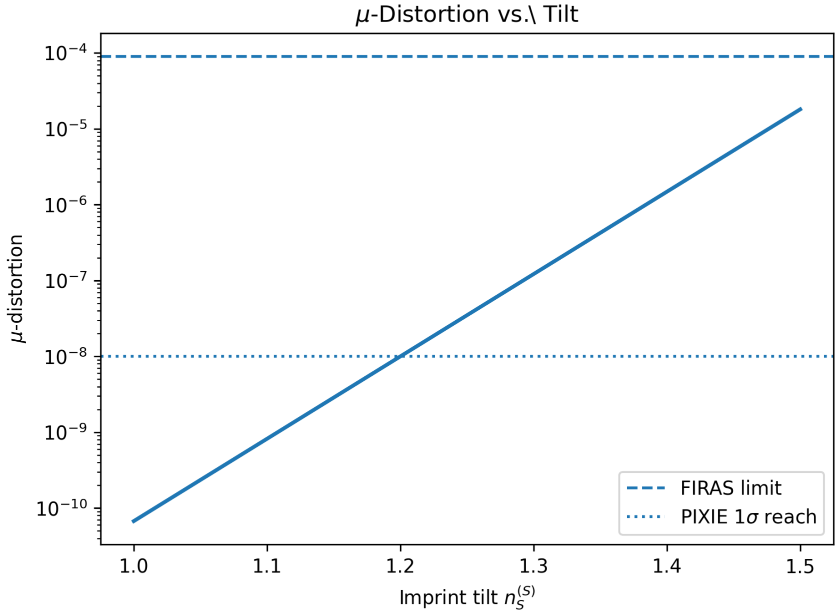

Figure 9. Chemical-potential distortion μ as a function of the imprint tilt $n_S^{(S)}$ for $\lambda = 1$. The dashed line marks the *FIRAS* 95 % upper limit ($|\mu| < 9 \times 10^{-5}$); the dotted line indicates the projected PIXIE 1σ sensitivity ($\sigma_\mu \simeq 10^{-8}$).

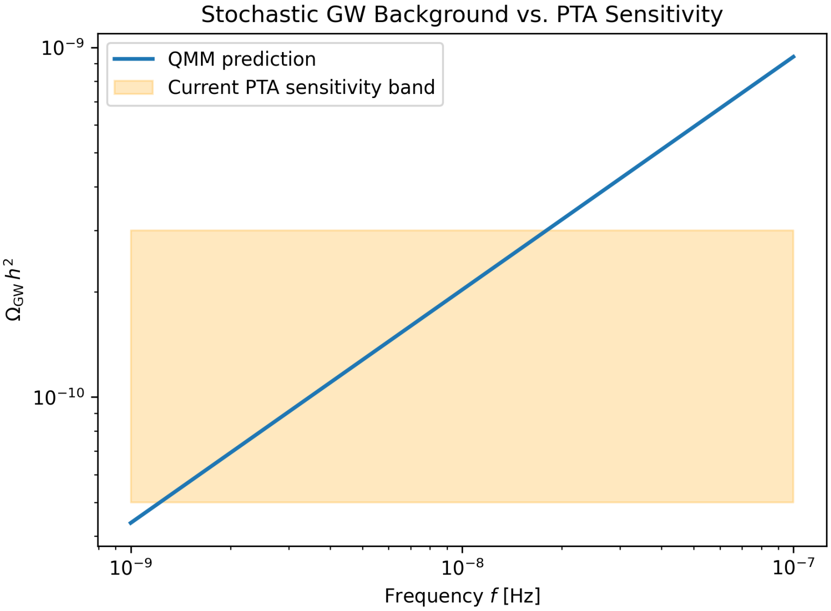

Figure 10. Predicted stochastic gravitational-wave background from QMM imprint dynamics (solid line) compared with the current PTA sensitivity band (shaded). The benchmark signal lies just below the NANOGrav 15-yr detection at $f \simeq 4$ nHz, placing PTAs at the forefront of near-term tests.

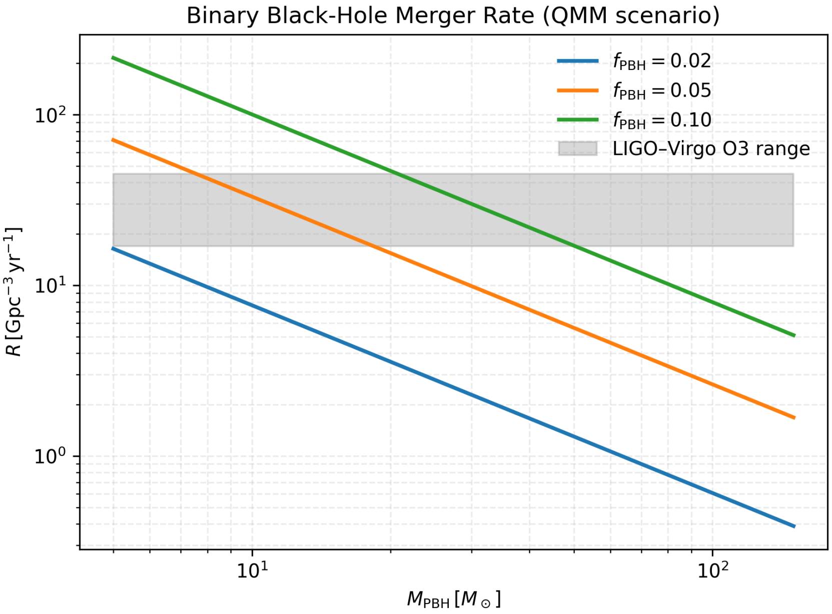

Figure 11. Predicted present-day binary-black-hole merger rate for three global PBH fractions f_{PBH}, shown over the mass range probed by LIGO-Virgo. The shaded band indicates the O3 90 % credible interval (17–45 $\mathrm{Gpc}^{-3}\,\mathrm{yr}^{-1}$).

Impact on first stars and reionization. For $M_{\text{PBH}} \gtrsim 10^2\, M_\odot$ the accretion luminosity exceeds L_{Edd} at $z \sim 30$, inflating H II regions and accelerating the formation of Pop-III stars [35]. Parameter choices with $n_S^{(S)} > 1.3$ predict such massive PBHs at $f_{\text{PBH}} \lesssim 5\%$, consistent with the *JWST* high-z UV luminosity function.

In summary, the QMM imprint-induced PBH scenario survives all current observational tests while offering near-term targets — μ-distortion, PTA GWs, and the redshift dependence of the merger rate — for a decisive confirmation or falsification.

8 Discussion

From curvature peaks to *information wells.* Traditional PBH scenarios engineer a sharp, transient rise in the curvature perturbation spectrum — via ultra-slow-roll phases, spectator fields, or tuned potential features — to trigger collapse when $\delta\rho/\rho$ exceeds the critical value δ_{c} [36, 37]. Such mechanisms demand delicate potential tuning and often run afoul of non-Gaussianity bounds. In the Quantum Memory Matrix (QMM) picture, by contrast, *information wells* are generic: imprint entropy is an unavoidable bookkeeping of every quantum interaction, and its spatial gradients gravitate like pressureless dust. The same field that cures the black-hole information paradox therefore seeds PBHs without sculpting the inflaton potential or amplifying curvature modes.

Economy of parameters. Only three dimensionless quantities govern phenomenology:

(i) the information-geometry coupling λ, which fixes the present-day fraction Ω_{QMM};

(ii) the bounce temperature T_{B}, which sets the k–M conversion [eq. (6.2)]; and

(iii) the small-scale tilt $n_S^{(S)}$, which controls the PBH mass spectrum.

Current CMB and large-scale-structure data constrain $\lambda = 1.0 \pm 0.3$ and $n_S^{(S)} < 1.4$ (95% C.L.). Forthcoming μ-distortion and PTA measurements will probe λ at the 10% level and push $n_S^{(S)}$ uncertainties below ± 0.05.

Open theoretical issues.

1. **Entropy decoherence.** How rapidly do imprint states decohere in a high-curvature bounce, and can such decoherence reshape $P_S(k)$?

2. **Quantum-classical crossover.** Is the stochastic treatment of $S(x)$ reliable once $(\nabla S)^2 \sim M_{\text{Pl}}^4$, or is a fully quantum-gravitational analysis required?

3. **Holographic saturation.** Finite Hilbert capacity per Planck cell implies a maximal imprint energy density. Does this cap prevent runaway collapse for very blue spectra?

Addressing these questions will decide whether QMM stands as a complete UV-extension of early-universe cosmology.

9 Conclusions

We have shown that the Quantum Memory Matrix endows a bouncing universe with *information wells* — overdensities produced by gradients in the imprint-entropy field $S(x)$. These wells grow linearly while outside the horizon and, upon re-entry, collapse into primordial black holes (PBHs) whose mass spectrum is dictated by just three parameters (λ, $n_S^{(S)}$, $T_{\rm B}$). For $\lambda \sim 1$ a mild blue tilt $n_S^{(S)} \simeq 1.2$ populates the LIGO-Virgo mass band (10–100 $M_\odot$); slightly steeper tilts yield sub-lunar PBHs that can constitute $\mathcal{O}(1)$ dark matter without violating microlensing constraints. Because the same imprint stress-energy modifies the integrated Sachs-Wolfe signal, generates μ-type CMB distortions, and sources a nanohertz gravitational-wave background, forthcoming CMB-S4, PIXIE, and PTA data provide decisive tests. If confirmed, the QMM framework would simultaneously explain dark matter, resolve the black-hole information puzzle, and account for the origin of PBHs — elevating *information* to a dynamical agent in cosmology and quantum gravity alike.

Acknowledgments

This research received no specific grant from any funding agency in the public, commercial, or not-for-profit sectors.

A Derivation of the QMM stress-energy tensor

Starting from $S_{\rm QMM} = \frac{\lambda}{2}\int d^4x\,\sqrt{-g}\,g^{\mu\nu}\partial_\mu S\,\partial_\nu S$, vary the action with respect to the metric:

$$\delta S_{\rm QMM} = \frac{\lambda}{2}\int d^4x\left[\sqrt{-g}\,\partial_\mu S\,\partial_\nu S\,\delta g^{\mu\nu} - \frac{1}{2}\sqrt{-g}\,g^{\mu\nu}\partial_\mu S\,\partial_\nu S\,g_{\alpha\beta}\,\delta g^{\alpha\beta}\right].$$

Using $\delta(\sqrt{-g}) = -\frac{1}{2}\sqrt{-g}\,g_{\alpha\beta}\,\delta g^{\alpha\beta}$ and lowering indices,

$$\delta S_{\rm QMM} = -\frac{1}{2}\int d^4x\,\sqrt{-g}\,T^{(\rm QMM)}_{\mu\nu}\,\delta g^{\mu\nu}, \qquad T^{(\rm QMM)}_{\mu\nu} = \lambda\left[\partial_\mu S\,\partial_\nu S - \frac{1}{2}g_{\mu\nu}(\partial S)^2\right].$$

Because S is a *dynamical* scalar, the Belinfante procedure allows one to add the identically conserved improvement term $\lambda(g_{\mu\nu}\Box S - \nabla_\mu\nabla_\nu S)$, yielding eq. (2.3) in the main text. Conservation follows directly from the Klein-Gordon equation $\Box S = 0$.

B Constraints on the imprint power spectrum

Planck TT+TE+EE+lowE+lensing data, combined with BOSS BAO, limit any dust-like component prior to matter-radiation equality to $\Omega_{\rm QMM}h^2 \leq 0.003$ (95 % CL) [8]. Because $\Omega_{\rm QMM} \propto \lambda A_S$ this implies

$$0.7 \lesssim \lambda\,A_S^{1/2} \lesssim 1.3 \quad (1\sigma).$$

Large-scale-structure power spectra from eBOSS and DES further restrict the blue tilt to $n_S^{(S)} \lesssim 1.4$ for $k \leq 1\,h\,\rm Mpc^{-1}$. These constraints are summarized in figure 12, which plots the allowed region in the $(\lambda, n_S^{(S)})$ plane and overlays contours of constant μ-distortion and present-day PBH fraction. The figure highlights in particular the sub-regions that yield (i) $\gtrsim$ 10% PBH dark matter, (ii) $\gtrsim$ 1% ISW excess, and (iii) $\mu > 3 \times 10^{-8}$.

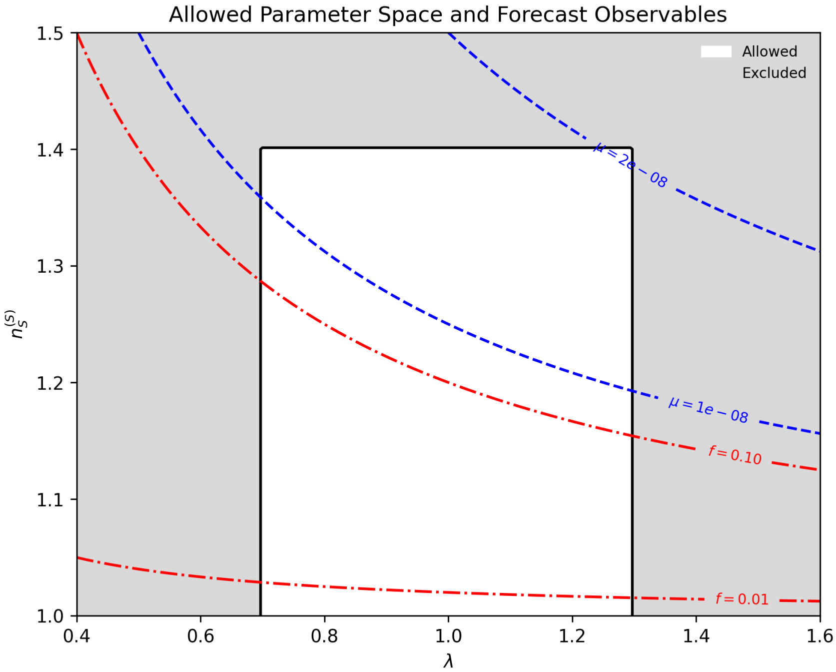

Figure 12. Allowed (white) and excluded (gray) regions in the $(\lambda, n_S^{(S)})$ plane after *Planck*+BAO+LSS constraints. Blue dashed contours indicate constant μ-distortion; red dash-dot contours show the present-day PBH fraction $f_{\rm PBH}$.

C PBH mass function details

The variance of the density contrast smoothed on scale R is

$$\sigma^2(R) = \lambda^2 \int \frac{dk}{k}\, P_S(k)\, W^2(kR),$$

where $W(kR) = 3[\sin(kR) - kR\cos(kR)]/(kR)^3$ is the real-space top-hat window. Critical collapse modifies the monochromatic approximation:

$$M = \kappa\, M_{\rm H}(\delta - \delta_{\rm c})^{\gamma_{\rm crit}}, \qquad \kappa \simeq 3.3,\ \gamma_{\rm crit} \simeq 0.36.$$

Transforming variables,

$$\beta(M) = \int_{\delta_{\rm c}}^{\infty} \frac{d\delta}{\sqrt{2\pi}\,\sigma} \exp\left[-\frac{\delta^2}{2\sigma^2}\right] \delta\big(M - \kappa M_{\rm H}(\delta - \delta_{\rm c})^{\gamma_{\rm crit}}\big).$$

A saddle-point expansion around $\delta_{\rm c}$ reproduces eq. (6.5) in leading order. The notebook computes $\beta(M)$, $\Omega_{\rm PBH}(M)$, and plots $f_{\rm PBH}$ against observational limits.

Remark. Section 6 shows that non-linear imprint feedback boosts the *final* PBH mass by a factor $B_{\rm acc} \sim 3 - 10$. All observational comparisons therefore use the mapping $M^{\rm final} = B_{\rm acc}\, M^{\rm form}$ after the monochromatic $\beta(M)$ is computed here.

D Numerical setup for bounce-to-PBH simulations

D.1 Modified Boltzmann code (CLASS/CAMB)

1. **New fluid.** Add a pressureless species `qmm` with energy density $\rho_{\mathrm{QMM}}(a) = \lambda(\dot{S}^2 + (\nabla S)^2/a^2)/2$.

2. **Perturbations.** Integrate eqs. (4.1) for each k in `perturb_sources.c`, sourcing metric potentials alongside CDM and baryons.

3. **Initial conditions.** Sample $P_S(k)$ at the bounce scale factor a_{B}, rescale to $a_{\mathrm{init}} = 10^{-8}$, and impose $\delta_{\mathrm{QMM}}(k, a_{\mathrm{init}}) = C_1(k)\, a_{\mathrm{init}}/a_{\mathrm{B}}$.

4. **Background module.** Insert $\rho_{\mathrm{QMM}}(a)$ into the Friedmann integrator; ensure the stiff term $\dot{S}^2$ is updated with a Runge-Kutta wrapper.

5. **Validation.** Recover ΛCDM spectra when $\lambda \to 0$ and replicate CAMB's ℓ-spectra within 0.1% for standard parameters.

D.2 N-body with live S-grid

- **Code base.** Fork Gadget-4 to include a lattice field S stored on the same PM grid as the density assignment.

- **Equations of motion.** Advance particles with $\ddot{\boldsymbol{x}} = -\nabla(\Phi + \Phi_{\mathrm{QMM}})$, where $\nabla^2 \Phi_{\mathrm{QMM}} = 4\pi G \rho_{\mathrm{QMM}}$; update ρ_{QMM} each step via $\rho_{\mathrm{QMM}} = \lambda[(\nabla S)^2 + a^2 \dot{S}^2]/2$.

- **Grid resolution.** $N_{\mathrm{grid}} = 2048^3$ for a $L = 500\, h^{-1}$Mpc box gives ~ 100 cells per comoving PBH Jeans length at $T_{\mathrm{re}} = 10^5$ GeV.

- **Time stepping.** Use a global $\Delta a = 2 \times 10^{-3}$ until $a = 10^{-2}$, then individual particle and field time steps satisfying $\Delta t \leq 0.02 H^{-1}$.

- **Convergence tests.** Halve Δa, double N_{grid}, and confirm PBH mass function changes $\leq 5\%$. Compare with one-dimensional high-resolution collapse to verify critical exponent recovery.

- **Grid resolution.** $N_{\mathrm{grid}} = 2048^3$ in a $L = 500\, h^{-1}$Mpc box still provides $\gtrsim 100$ cells per comoving PBH Jeans length for the fiducial $T_{\mathrm{B}} = 10^5$ GeV benchmark.

Supplementary notebook. All analysis code and data products are provided in the Jupyter file available in the Supplementary Material (`QMM_PBH.ipynb`), which reproduces the figures and numerical results. Executing the notebook regenerates figures 1–12, reproduces the $(\lambda, n_S^{(S)})$ constraints in appendix B, and outputs machine-readable tables of the PBH mass function and merger-rate predictions.

References

[1] Y.B. Zel'dovich and I.D. Novikov, *The hypothesis of cores retarded during expansion and the hot cosmological model*, *Sov. Astron.* **10** (1967) 602 [INSPIRE].

[2] S. Hawking, *Gravitationally collapsed objects of very low mass*, *Mon. Not. Roy. Astron. Soc.* **152** (1971) 75 [INSPIRE].

[3] B.J. Carr and S.W. Hawking, *Black holes in the early universe*, *Mon. Not. Roy. Astron. Soc.* **168** (1974) 399 [INSPIRE].

[4] B. Carr and F. Kühnel, *Primordial black holes as dark matter: recent developments*, *Ann. Rev. Nucl. Part. Sci.* **70** (2020) 355 [`arXiv:2006.02838`] [INSPIRE].

[5] R. Brandenberger and P. Peter, *Bouncing cosmologies: progress and problems*, *Found. Phys.* **47** (2017) 797 [`arXiv:1603.05834`] [INSPIRE].

[6] D. Dubbers et al., *Exotic decay channels are not the cause of the neutron lifetime anomaly*, *Phys. Lett. B* **791** (2019) 6 [`arXiv:1812.00626`] [INSPIRE].

[7] I. Musco, *Threshold for primordial black hole formation*, in *Proceedings of the 14th Marcel Grossmann meeting*, World Scientific, Singapore (2017), p. 11.

[8] Planck collaboration, *Planck 2018 results. VI. Cosmological parameters*, *Astron. Astrophys.* **641** (2020) A6 [*Erratum ibid.* **652** (2021) C4] [`arXiv:1807.06209`] [INSPIRE].

[9] F. Neukart, *Geometry-information duality: quantum entanglement contributions to gravitational dynamics*, *Annals Phys.* **479** (2025) 170044 [`arXiv:2409.12206`] [INSPIRE].

[10] F. Neukart, R. Brasher and E. Marx, *The quantum memory matrix: a unified framework for the black hole information paradox*, *Entropy* **26** (2024) 1039 [`arXiv:2504.00039`] [INSPIRE].

[11] F. Neukart, E. Marx and V. Vinokur, *Planck-scale electromagnetism in the quantum memory matrix: a discrete approach to unitarity*, (2025) [`DOI:10.20944/preprints202503.0551.v1`].

[12] F. Neukart, E. Marx and V. Vinokur, *Extending the QMM framework to the strong and weak interactions*, *Entropy* **27** (2025) 153 [`arXiv:2504.03817`] [INSPIRE].

[13] F. Neukart, *Quantum entanglement asymmetry and the cosmic matter-antimatter imbalance: a theoretical and observational analysis*, *Entropy* **27** (2025) 103 [INSPIRE].

[14] S.M. Carroll, *Spacetime and geometry: an introduction to general relativity*, Addison-Wesley, San Francisco, CA, U.S.A. (2004).

[15] L.D. Landau and E.M. Lifshitz, *The classical theory of fields*, fourth edition, Pergamon Press, Oxford, U.K. (1975).

[16] V. Mukhanov, *Physical foundations of cosmology*, Cambridge University Press, Cambridge, U.K. (2005).

[17] N. Deruelle and V.F. Mukhanov, *On matching conditions for cosmological perturbations*, *Phys. Rev. D* **52** (1995) 5549 [`gr-qc/9503050`] [INSPIRE].

[18] Y.-F. Cai, D.A. Easson and R. Brandenberger, *Towards a nonsingular bouncing cosmology*, *JCAP* **08** (2012) 020 [`arXiv:1206.2382`] [INSPIRE].

[19] E. Wilson-Ewing, *Ekpyrotic loop quantum cosmology*, *JCAP* **08** (2013) 015 [`arXiv:1306.6582`] [INSPIRE].

[20] E.M. Barboza, R.C. Nunes, E.M.C. Abreu and J.A. Neto, *Thermodynamic aspects of dark energy fluids*, *Phys. Rev. D* **92** (2015) 083526 [`arXiv:1501.03491`] [INSPIRE].

[21] M. Novello and S.E.P. Bergliaffa, *Bouncing cosmologies*, *Phys. Rept.* **463** (2008) 127 [arXiv:0802.1634] [INSPIRE].

[22] T. Harada, C.-M. Yoo and K. Kohri, *Threshold of primordial black hole formation*, *Phys. Rev. D* **88** (2013) 084051 [*Erratum ibid.* **89** (2014) 029903] [arXiv:1309.4201] [INSPIRE].

[23] M.W. Choptuik, *Universality and scaling in gravitational collapse of a massless scalar field*, *Phys. Rev. Lett.* **70** (1993) 9 [INSPIRE].

[24] J.C. Niemeyer and K. Jedamzik, *Dynamics of primordial black hole formation*, *Phys. Rev. D* **59** (1999) 124013 [astro-ph/9901292] [INSPIRE].

[25] M. Shibata and M. Sasaki, *Black hole formation in the Friedmann universe: formulation and computation in numerical relativity*, *Phys. Rev. D* **60** (1999) 084002 [gr-qc/9905064] [INSPIRE].

[26] B.J. Carr, *The primordial black hole mass spectrum*, *Astrophys. J.* **201** (1975) 1 [INSPIRE].

[27] A.M. Green and B.J. Kavanagh, *Primordial black holes as a dark matter candidate*, *J. Phys. G* **48** (2021) 043001 [arXiv:2007.10722] [INSPIRE].

[28] D.J. Fixsen et al., *The cosmic microwave background spectrum from the full COBE FIRAS data set*, *Astrophys. J.* **473** (1996) 576 [astro-ph/9605054] [INSPIRE].

[29] NANOGrav collaboration, *The NANOGrav 15 yr data set: evidence for a gravitational-wave background*, *Astrophys. J. Lett.* **951** (2023) L8 [arXiv:2306.16213] [INSPIRE].

[30] H. Niikura et al., *Microlensing constraints on primordial black holes with Subaru/HSC Andromeda observations*, *Nature Astron.* **3** (2019) 524 [arXiv:1701.02151] [INSPIRE].

[31] L. Wyrzykowski et al., *The OGLE view of microlensing towards the Magellanic clouds. IV. OGLE-III SMC data and final conclusions on MACHOs*, *Mon. Not. Roy. Astron. Soc.* **416** (2011) 2949 [arXiv:1106.2925] [INSPIRE].

[32] S. Bird et al., *Did LIGO detect dark matter?*, *Phys. Rev. Lett.* **116** (2016) 201301 [arXiv:1603.00464] [INSPIRE].

[33] Y. Ali-Haïmoud and M. Kamionkowski, *Cosmic microwave background limits on accreting primordial black holes*, *Phys. Rev. D* **95** (2017) 043534 [arXiv:1612.05644] [INSPIRE].

[34] LIGO Scientific and Virgo collaborations, *Binary black hole population properties inferred from the first and second observing runs of advanced LIGO and advanced Virgo*, *Astrophys. J. Lett.* **882** (2019) L24 [arXiv:1811.12940] [INSPIRE].

[35] S.M. Koushiappas and A. Loeb, *Dynamics of dwarf galaxies disfavor stellar-mass black holes as dark matter*, *Phys. Rev. Lett.* **119** (2017) 041102 [arXiv:1704.01668] [INSPIRE].

[36] P. Ivanov, P. Naselsky and I. Novikov, *Inflation and primordial black holes as dark matter*, *Phys. Rev. D* **50** (1994) 7173 [INSPIRE].

[37] M.S. Madhavacheril, N. Battaglia, K.M. Smith and J.L. Sievers, *Cosmology with the kinematic Sunyaev-Zeldovich effect: breaking the optical depth degeneracy with fast radio bursts*, *Phys. Rev. D* **100** (2019) 103532 [arXiv:1901.02418] [INSPIRE].

[38] J. Lesgourgues, *The Cosmic Linear Anisotropy Solving System (CLASS) I: overview*, arXiv:1104.2932 [INSPIRE].

[39] A. Lewis, A. Challinor and A. Lasenby, *Efficient computation of CMB anisotropies in closed FRW models*, *Astrophys. J.* **538** (2000) 473 [astro-ph/9911177] [INSPIRE].

[40] V. Springel, R. Pakmor, O. Zier and M. Reinecke, *Simulating cosmic structure formation with the gadget-4 code*, *Mon. Not. Roy. Astron. Soc.* **506** (2021) 2871 [arXiv:2010.03567] [INSPIRE].

[41] M. Sasaki, T. Suyama, T. Tanaka and S. Yokoyama, *Primordial black holes — perspectives in gravitational wave astronomy*, *Class. Quant. Grav.* **35** (2018) 063001 [`arXiv:1801.05235`] [INSPIRE].

[42] B. Carr, F. Kuhnel and M. Sandstad, *Primordial black holes as dark matter*, *Phys. Rev. D* **94** (2016) 083504 [`arXiv:1607.06077`] [INSPIRE].

[43] D. Álvarez-Ortega, G.J. Olmo, D. Rubiera-García and D. Gómez Sáez-Chillón, *Eternal versus singular observers in interacting dark-energy-dark-matter models*, *Phys. Rev. D* **106** (2022) 023523 [`arXiv:2204.11676`] [INSPIRE].

[44] B. Carr, K. Kohri, Y. Sendouda and J. Yokoyama, *Constraints on primordial black holes*, *Rept. Prog. Phys.* **84** (2021) 116902 [`arXiv:2002.12778`] [INSPIRE].

[45] LIGO SCIENTIFIC and VIRGO collaborations, *GWTC-2: compact binary coalescences observed by LIGO and Virgo during the first half of the third observing run*, *Phys. Rev. X* **11** (2021) 021053 [`arXiv:2010.14527`] [INSPIRE].